Impact of the F– for O2– substitution in Na3V2(PO4)2F3–yOy on their transport properties and electrochemical performance

Runhe Fang, Jacob Olchowka, Chloé Pablos, Rafael Bianchini Nuernberg, Laurence Croguennec, Sophie Cassaignon

Impact of the F^- for O^{2-} substitution in $Na_3V_2(PO_4)_2F_{3-y}O_y$ on their transport properties and electrochemical performance

Runhe Fang [a,d], Jacob Olchowka [b,d,e,*], Chloé Pablos [b,c,d], Rafael Bianchini Nuernberg [b], Laurence Croguennec [b,d,e], Sophie Cassaignon[a,d,*]

[a] Sorbonne Université, CNRS, Laboratoire Chimie de la Matière Condensée de Paris, LCMCP, UMR 7574, 4 Place Jussieu, 75005 Paris, France

[b] Univ. Bordeaux, CNRS, Bordeaux INP, ICMCB, UMR 5026, F-33600 Pessac, France

[c] Laboratoire de Réactivité et de Chimie des Solides, Université de Picardie Jules Verne, CNRS-UMR 7314, F-80039 Amiens Cedex 1, France

[d] RS2E, Réseau Français sur le Stockage Electrochimique de l'Energie, CNRS 3459, 80039 Amiens Cedex 1, France.

[e] ALISTORE-ERI European Research Institute, CNRS 3104, 80039 Amiens Cedex 1, France

Abstract:

The series of polyanionic compounds $Na_3V^{3+}_{2-y}V^{4+}_y(PO_4)_2F_{3-y}O_y$ ($0 \leq y \leq 2$) attracts much attention as positive electrode material for Na-ion batteries, because of its high operating potential and stable cycling performance. A series of nanospherical $Na_3V^{3+}_{2-y}V^{4+}_y(PO_4)_2F_{3-y}O_y$ ($NVPFO_y$) materials with y = 0.8, 1.35, 1.6 and 2 was synthesized using a solvothermal reaction and changes in the vanadium average oxidation state were fully characterized combining analyses by Raman and infrared spectroscopies and X-ray diffraction. Raman spectroscopy, beyond checking for the absence of a carbon coating, was in fact used for its sensitivity to the vanadium environment and turn out to be an efficient characterization technique to estimate the oxygen content within the $Na_3V^{3+}_{2-y}V^{4+}_y(PO_4)_2F_{3-y}O_y$ family. The impact of the oxygen content on the transport properties was evaluated by electrochemical impedance spectroscopy. The material with y = 1.35 demonstrates the smallest electrical resistivity in the series, as well as the best rate capability and cyclability upon long-term cycling, despite no carbon coating and a high mass loading positive electrode.

KEYWORDS: Na-ion batteries; Polyanionic positive electrode materials; $Na_3V_2(PO_4)_2F_3$; $Na_3(VO)_2(PO_4)_2F$; Transport properties; Raman spectroscopy.

* Corresponding authors:

S. Cassaignon (sophie.cassaignon@sorbonne-universite.fr)

J. Olchowka (jacob.olchowka@icmcb.cnrs.fr)

1. Introduction

As the climate problem grows, the European Union, like many political entities all over the world, proposed to reach the climate-neutral by 2050, which means reaching net zero greenhouse gas emissions with the help of European climate law.[1] This ambition inevitably requires reducing the consumption of fossil fuel energy and strongly enhances solar and wind energy production. However, due to their intermittent character, these latter can be efficient only when coupled with performant energy storage devices that can store the excess of production and reinject it into the grid during peak demands. Sodium-ion batteries are believed to be a reliable and environmentally friendly energy storage system to respond this problem.[2–4] Among all the materials tested as positive electrode materials, such as layered oxides and polyanionic ones, the series of $Na_3V^{3+}_{2-y}V^{4+}_{y}(PO_4)_2F_{3-y}O_y$ ($0 \leq y \leq 2$) ($NVPFO_y$) is one of the most promising due to its high operating voltage, long cycling stability and low volume changes upon the extraction/insertion of two Na^+ ions per formula unit.[5–8]

The three-dimensional framework of this family is made of $V_2O_8F_{3-y}O_y$ bi-octahedral units interlinked together by PO_4 tetrahedra that allows efficient 2D Na^+ diffusion within tunnels along the [110] and $[1\bar{1}0]$ directions.[9] Unfortunately, although the phosphates contribute largely to stabilize the structure during cycling, they isolate the metal ions that begets a rather poor intrinsic electronic conductivity which reduces significantly the performance, especially at high rates. Such as it was done for $LiFePO_4$, many remedies are proposed to improve the rate capabilities, such as combining $NVPFO_y$ with conductive carbon source (carbon coating, carbon nanotube, graphene etc.),[10–18] performing an elemental substitution (Al, Fe, Mn etc.)[19–22], and designing nanostructured morphologies [13,23–27]. However, few studies have been done to evaluate the intrinsic conductivity within the $Na_3V^{3+}_{2-y}V^{4+}_{y}(PO_4)_2F_{3-y}O_y$ series depending on oxygen content. Broux et al. demonstrated that a low partial substitution of O^{2-} for F^- (when the composition changes from $Na_3V_2(PO_4)_2F_3$ (y = 0) to $Na_3V_2(PO_4)_2F_{2.5}O_{0.5}$ (y = 0.5)) could improve both the electronic and ionic conductivities (at 95°C, from 1.22×10^{-10} to 3.76×10^{-10} $S.cm^{-1}$ and 4.98×10^{-10} to 6.38×10^{-10} $S.cm^{-1}$, respectively).[28] Park et al. performed high temperature measurements (> 430 K) and estimated, by interpolation, a room temperature electrical conductivity close to 2.4×10^{-12} $S.cm^{-1}$ for $Na_3V_2(PO_4)_2F_{1.4}O_{1.60}$ (y = 1.60).[29] Similarly, it is reported that the O^{2-} for F^- substitution improves the ionic conductivity of Na^+ and stabilizes the structure during the overcharge.[30,31] Dealing with electrochemical performances, Qi et al. reported that higher rate capability is achieved for $Na_3V^{3+}_2(PO_4)_2FO_2$ (y = 2) compared to $Na_3V^{4+}_2(PO_4)_2F_3$ (y = 0), possibly due to a faster Na^+ diffusion[32]. However,

few is known whether a mixed V^{3+}/V^{4+} pristine composition could be of benefit or not for high rate charge/discharge.

In this work, four compounds of the $Na_3V^{3+}_{2-y}V^{4+}_{y}(PO_4)_2F_{3-y}O_y$ series, and possessing different O/F ratios, were synthesized using solvothermal reactions. Their chemical composition was carefully determined by X-ray diffraction and a combination of spectroscopic techniques, whereas microscopy imaging confirmed that the same spherical morphology was obtained for all the members of the series. Electrochemical impedance spectroscopy analyses and electrochemical tests, including high rates and long range cycling, were performed to investigate the influence of the chemical composition of $NVPFO_y$ on their electronic conductivity and energy storage performance. Moreover, these analyses were carried out on electrodes with high mass loading of active material (88 wt.%) prepared without any carbon coating, with the aim to better determine the oxygen content impact on the electrochemical properties in conditions as close as possible to practical conditions.

2. Experimental Section

2.1 Materials preparation

A series of $Na_3V^{3+}_{2-y}V^{4+}_{y}(PO_4)_2F_{3-y}O_y$ ($NVPFO_y$) compounds was prepared via an easy one-step solvothermal reaction. First, appropriate amounts (molar ratio) of vanadium acetylacetonate (Sigma-Aldrich; ≥ 97%) ($V(acac)_3$), vanadyl acetylacetonate (Sigma-Aldrich; ≥ 97%) ($VO(acac)_3$), sodium fluorine (Prolabo; 98%) and phosphoric acid (VWR; 85%) were introduced into 100 mL Teflon Parr autoclave containing an equimolar mixture water/ethanol (**Table 1**) and stirred for 10 min. Then, the mixtures were heated in an oven at 180°C during 10 h. Finally, polycrystalline powders, presenting various shades of green (**Figure S1**), were retrieved through complete cleaning by centrifugation (firstly with ethanol, then with distilled water) and a full drying in vacuum at 60°C overnight. As detailed in **Table 1**, stoichiometric amount of NaF and H_3PO_4 were used according to reference [33] in order to obtain nanospherical morphology, which shows extremely promising performance. The phase obtained from the precursors' molar ratio of 0.25 $VO(acac)_2$: 0.75 $V(acac)_3$ possesses, according to the Rietveld refinement and spectroscopic studies, similar composition to $NVPFO_{0.8}$ (see **Figure S2** in supplementary information for more details). Thus, due to a rather oxidative environment, these synthesis conditions would lead to a minimum average oxidation state of 3.4 for vanadium in the final product, with at least 0.8 V^{4+} among 2 per formula unit. The vanadium oxidation during solvothermal synthesis was already observed in our previous work.[33]

Table 1: Detailed molar ratios and synthesis conditions used to prepare all the studied materials.

Type	$VO(acac)_2$	$V(acac)_3$	NaF	H_3PO_4	Ethanol solution	T	Time
$NVPFO_{0.80}$	0	1	1.5	1	50%	180°C	10H
$NVPFO_{1.35}$	0.50	0.50	1.5	1	50%	180°C	10H
$NVPFO_{1.60}$	0.75	0.25	1.5	1	50%	180°C	10H
$NVPFO_2$	1	0	1.5	1	50%	180°C	10H

2.2 Characterization techniques

X-ray diffraction (XRD) measurements were carried out by using a BRUKER D8 ADVANCE diffractometer in θ-θ configuration, equipped with a Cu $K_{\alpha 1,2}$ X-ray source. The acquisition was performed in the 2θ angular range of 10° – 140° with a step size of 0.0197°. The Rietveld refinements were performed using the FullProf Suite.[34]

Scanning electron microscopy (SEM) images were taken without any conductive deposition by a Hitachi Model S-3400N microscope and SEM-FEG (field emission gun) images were obtained on a Hitachi SU-70 microscope. Transmission electron microscopy (TEM) analyses were carried out with the Tecnai spirit G2 microscope. The powder was sonificated for 20 min in ethanol before the analysis.

Fourier transformed infrared (FT-IR) spectra were recorded by using a PerkinElmer Spectrum 400 FT-IR/FT-NIR spectrometer in the wavenumber range of 400 - 4000 cm^{-1} (mid-IR). Raman spectra were obtained with a confocal LabRAM HR Evolution micro-spectrometer from Horiba, using a 633 nm laser source. They were collected in the range 100-1300 cm^{-1}, using a 10.6 mm (NA 0.5) focal length lens and with an acquisition time of 20 s and 40 accumulations. Additional acquisitions were performed between 450-600 cm^{-1} and 850-1100 cm^{-1} in order to reach a better resolution in these wavenumber ranges.

The electrical properties of $Na_3V_2(PO_4)_2F_{3-y}O_y$ compounds were investigated by electrochemical impedance spectroscopy (EIS). For this purpose, the powders were mixed with camphor (about 2 wt.%) and pressed into pellets of 13 mm diameter applying 200 MPa by means of a uniaxial press. Subsequently, the pellets were heat-treated at 250 °C for 1 h under air to evaporate the camphor. Then, gold electrodes were sputtered on their parallel opposite faces to ensure electrical contact. EIS measurements were performed at OCP using a Solartron 1260 Impedance/Gain Phase Analyzer in the frequency range between 1 MHz and 1Hz, with an applied root mean square voltage of 100 mV, 10 points per decade and 20 measures per point.

The measurements were carried out in air, using a two-probe sample-holder and over the temperature range of 100 - 300 ºC.

The electrochemical performances of the materials were tested in CR2032-type coin cells. The positive electrodes were prepared as a mixture containing the active material, carbon black, and polyvinylidene fluoride (PVDF) in NMP (N-Methyl-2-pyrrolidone) with the ratio of 88/7/5 (by wt.%). After an hour of thorough mixing, the black ink was casted as a flat film by doctor blade on an aluminum foil and dried in an oven at 60°C. Disks were cut, then pressed under 5 tons and finally dried overnight at 80ºC under vacuum. A homemade electrolyte containing a 1 $mol.L^{-1}$ solution of $NaPF_6$ (Strem Chemical; 99%) in ethylene carbonate and dimethyl carbonate (EC/DMC = 1/1) with 2 wt.% of fluoroethylene carbonate (FEC) was used for all the electrochemical tests. The assembled cells were cycled in galvanostatic mode, from C/20 to 2C cycling rates between 2.5 and 4.3 V vs. Na^+/Na. The theoretical capacity being 128 $mAh.g^{-1}$ (corresponding to 2 Na^+ reversibly extracted from $NVPFO_2$), the rate C/20 corresponds to the exchange of 2 Na^+ in 20 hours. The electrodes have a typical active mass loading around 5 $mg.cm^{-2}$. The tests were performed several time and **Figure S3** shows an example of reproducibility.

3. Results and discussions

3.1 Structural and morphological characterization

The XRD patterns obtained for all the compounds synthesized by solvothermal method indicate the successful syntheses of pure phases that belong to the solid solution $Na_3V^{3+}_{2-y}V^{4+}_y(PO_4)_2F_{3-y}O_y$ (**Figure 1a**). The lattice parameters determined from the Rietveld refinement are reported in **Table 2** and the results of these refinements are presented in **Figures S1**.[9,30]

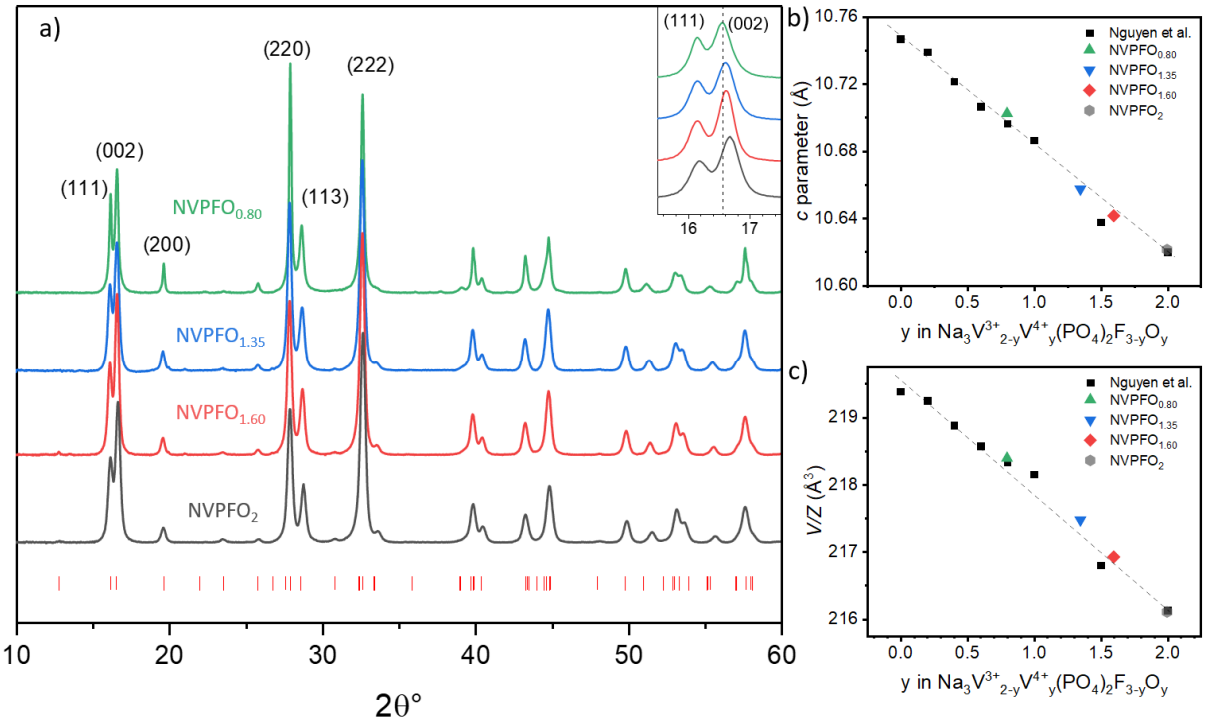

Figure 1. a) X-ray diffraction patterns of $NVPFO_{0.80}$, $NVPFO_{1.35}$, $NVPFO_{1.60}$ and $NVPFO_2$. The red ticks correspond to theoretical positions as reported in ICDD 00-066-0322. b-c) Comparison of the c-cell parameters and V/Z values (V/Z being the cell volume per formula unit) as determined for these four compounds by Rietveld refinement with those already reported in ref[30]. The dash lines give the evolution of these parameters as a function of y in $Na_3V_2(PO_4)_2F_{3-y}O_y$.

The structure of $Na_3V_2(PO_4)_2F_3$ is built from $V_2O_8F_3$ bi-octahedral units linked to each other by phosphate groups to generate a 3D framework. Each bi-octahedron is composed by two VO_4F_2 octahedra sharing a common fluorine. The fluorine atoms are in apical positions (along the c-axis) and the oxygen atoms in the equatorial plane.[35] The substitution of F^- anions that are pointing outside the bi-octahedra by O^{2-} induces vanadium oxidation from V^{3+} to V^{4+} and formation of short covalent V=O bonds (~1.6 Å) instead of long ionic V-F bonds (~2 Å) (**Figure S4**).[36] Thus, as reported by Park et al. and Nguyen et al., it is possible to determine the chemical composition of the $NVPFO_y$ family members from the *c*-cell parameter and V/Z value, the cell volume per formula unit, due to their linear evolution within the solid solution $Na_3V^{3+}_{2-y}V^{4+}_y(PO_4)_2F_{3-y}O_y$ ($0 \leq y \leq 2$).[8,30] For instance, in **Figure 1a** (insert), it can be clearly seen a shift of the *(002)* reflection to higher 2θ values when increasing the ratio of V^{4+}/V^{3+} precursors, which according to Bragg law leads to a decrease of the *c*-cell parameter. Based on the lattice parameters determined from Rietveld refinement, the syntheses lead to the preparation of $Na_3V^{3+}_{1.20}V^{4+}_{0.80}(PO_4)_2F_{2.20}O_{0.80}$ ($NVPFO_{0.80}$), $Na_3V^{3+}_{1.65}V^{4+}_{1.35}(PO_4)_2F_{1.65}O_{1.35}$ ($NVPFO_{1.35}$), $Na_3V^{3+}_{1.40}V^{4+}_{1.60}(PO_4)_2F_{1.40}O_{1.60}$ ($NVPFO_{1.60}$) and $Na_3V^{4+}_2(PO_4)_2FO_2$ ($NVPFO_2$) (**Table 2**, **Figures 1a-c** and **S1**). It can be noticed that due to the oxidative character of the solvent (water/ethanol mixture), V^{3+} is partially oxidized during the synthesis, which leads to

compounds with vanadium mean oxidation state higher to the one expected from the reactants' ratio. This oxidation in hydrothermal conditions was already reported in several works and highlights the difficulty to precisely control the chemical composition within this polyanionic series, especially for F^--rich members.[33,37–39]

Table 2: Lattice parameters obtained by the Rietveld refinement of the XRD patterns, coherent domain sizes along the (220) and (002) directions, and chemical compositions determined for all the NVPFO$_y$ materials.

	a (Å)	b (Å)	c (Å)	V/Z (Å^3)	(220) (nm)	(002) (nm)	Formula	Space group
$NVPFO_{0.80}$	9.0375(1)	9.0382(1)	10.7014(1)	218.53(1)	44	34	$Na_3V^{3+}_{1.20}V^{4+}_{0.80}(PO_4)_2F_{2.20}O_{0.80}$	Amam
$NVPFO_{1.35}$	9.0347(1)	9.0347(1)	10.6571(2)	217.47(1)	28	23	$Na_3V^{3+}_{0.65}V^{4+}_{1.35}(PO_4)_2F_{1.65}O_{1.35}$	P42/mnm
$NVPFO_{1.60}$	9.0299(1)	9.0299(1)	10.6412(2)	216.92(1)	25	26	$Na_3V^{3+}_{0.40}V^{4+}_{1.60}(PO_4)_2F_{1.40}O_{1.60}$	P42/mnm
$NVPFO_2$	9.0215(1)	9.0215(1)	10.6210(3)	216.10(1)	22	24	$Na_3V^{4+}_2(PO_4)_2FO_2$	P42/mnm

Infrared spectroscopy measurements reveal the presence of bands at ~675 cm^{-1} and ~1050 cm^{-1} corresponding to the vibrations of V-O bonds and phosphate groups respectively. Additionally, bands associated to vanadyl bonds are observed for the four compounds with the systematic presence of sharp signals at 915 and 940 cm^{-1}, characteristic of the vibrations generated by covalent V=O bonds (**Figure 2a**). Nguyen et al. suggested that the presence of these two $\nu_{V=O}$ bands is consistent with two different local environments for the vanadyl bond.[30] The band at 940 cm^{-1} (Band B) would correspond to a V^{4+}=O bond with a V^{3+}-F bond opposite along the axis of the bi-octahedral unit, whereas the one at 915 cm^{-1} (Band A) involves the presence of two V^{4+}=O bonds in the same bi-octahedra. Thus, the relative intensity observed between the two V=O vibration bands tends to match the variation of the vanadium average oxidation state determined by X-ray diffraction: the higher the Band A (V^{4+}-V^{4+} bi-octahedra) / Band B (V^{4+}-V^{3+} bi-octahedra) ratio, the higher the vanadium mean oxidation state (**Figure 2b**).

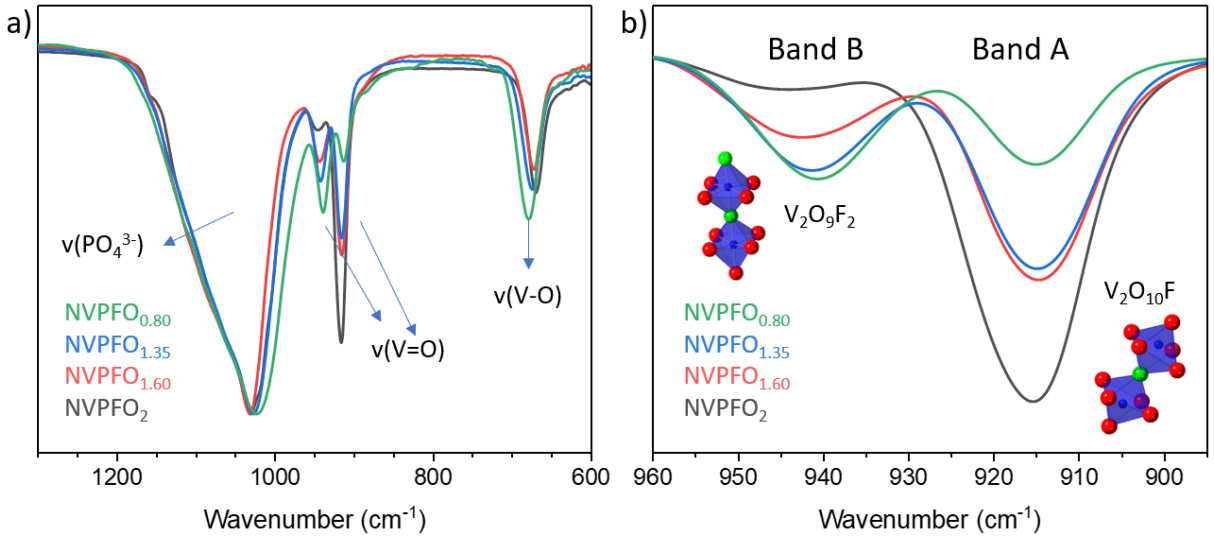

Figure 2. FTIR spectroscopy analyses: a) The intensities of the spectra were normalized to the signal attributed to vibration of phosphate groups at ~1050 cm^{-1} to highlight the evolution of the intensities attributed to the vibrations of V=O bond, depending on its concentration, and b) Focus between 890 and 960 cm^{-1} to better observe the evolution of V=O bonds.

Complementary to Infrared spectroscopy, Raman spectroscopy is another efficient method to probe the local environments within materials.[40] To the best of our knowledge, this technique is, up to now, used mainly to characterize graphitization degree of the carbon coating applied on $NVPFO_y$ to enhance the electronic conductivity of the electrode material,[24,41] whereas it could give precious information on vanadium environment. **Figure S5** exhibits the Raman spectra of all compounds obtained with a 633 nm laser source between 100 and 1300 cm^{-1}, while **Figure 3** shows the enlarged areas that will be discussed here more in details. On **Figure 3a,** the signal around 940 cm^{-1} is attributed to V=O vibrations whereas the broad band at ~1050 cm^{-1} is characteristic of phosphate vibrations.[42,43] This attribution is supported by absence of band at 940 cm^{-1} for $Na_3V_2(PO_4)_2F_3$ which does not possess vanadyl bond (**Figure S6**). Within $NVPFO_y$ series, the intensity of the peak at 940 cm^{-1} increases continuously with the concentration of vanadyl bonds as determined from X-ray diffraction, which demonstrates the possibility to estimate whether the composition is V^{3+}-rich or V^{4+}=O-rich by analyzing the intensity ratio between the vanadyl and phosphate bands (**Table 3**). Additionally, the low intensity signal at 900 cm^{-1} (* in the **Figure 3**) observed for $NVPFO_{0.80}$ disappears for the more oxidized compositions, which may reveal a change in structure symmetry. This is in perfect agreement with the work of Nguyen et al., which reported a clear orthorhombic distortion in $NVPFO_y$ series for $y \leq 1$, whereas a tetragonal symmetry could be considered for phases with $y > 1$.[30] Besides, the intensity of the vibration peak generated by V-O bond (**Figure 3b)** is gradually decreasing and accompanied by a right ward shift from 525 to 532 cm^{-1} with the increase of vanadium mean oxidation state.[42] Indeed, this linear displacement can be perfectly explained by the increase of V^{n+}-O bond covalency upon metal ion oxidation and the position of the band can thus be used to estimate the vanadium mean oxidation state and hence the chemical formula within the solid solution (**Figure S7**). Thus, Raman spectroscopy appears to be an efficient complementary technique to confirm the $Na_3V^{3+}_{2-y}V^{4+}_y(PO_4)_2F_{3-y}O_y$ ($0 \leq y \leq 2$) composition deduced by X-ray diffraction and although theoretical calculations would be needed to attribute each signal, it could help to alleviate doubts about symmetry in this series.[9]

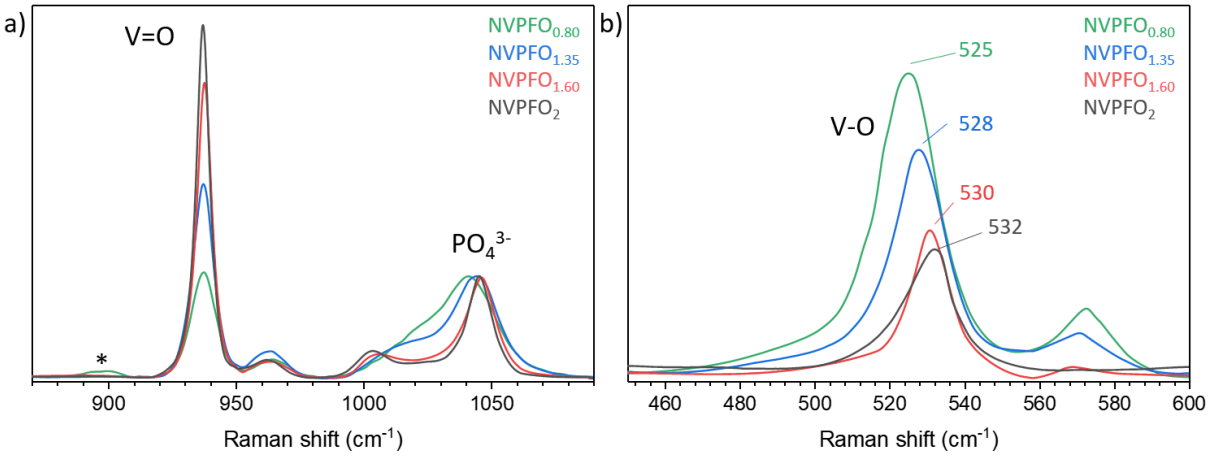

Figure 3. a) Raman spectra collected for $NVPFO_{0.80}$, $NVPFO_{1.35}$, $NVPFO_{1.60}$ and $NVPFO_2$: The intensities of the spectra were normalized to the signal attributed to the vibration of phosphate groups at ~1050 cm^{-1} to highlight the evolution of the intensity attributed to the vibration of V=O bond depending on its concentration, and b) focus between 450 and 600 cm^{-1} to observe the evolution of the band attributed to vibration of V-O bonds.

Table 3: Absolute intensity ratios of the V=O vibration and PO_4^{3-} vibration for all the materials studied

	$NVPFO_{0.80}$	$NVPFO_{1.35}$	$NVPFO_{1.60}$	$NVPFO_2$
Intensity ratio $\nu_{V=O} : \nu_{P-O}$	1.04	1.90	2.90	3.49

SEM images (**Figure 4**) show that all the compounds unveil micrometric aggregates made of spherical particles with diameters distributed between 200 and 400 nm and present very similar particle size distribution according to the histogram illustrating the statistics of particle sizes (**Figure S8**). Complementary analyses by high resolution SEM-FEG reveal that these spherical particles are mainly composed of smaller spheres of about 30 nm diameter. Furthermore, HRTEM analyses (**Figure 5**) and spacing measurements of lattice fringes confirm that these primary particles of 20-30 nm are $NVPFO_y$ crystallites, which perfectly fits to the crystallite size determined by XRD using Scherrer equation (**Table 2**). According to a recent work that reports a study dealing with the influence of $NVPFO_y$ particle's morphology on energy storage performance, spherical aggregates composed of nanospherical particles allow an optimal access to the Na^+ diffusion channels and should be favored to reach the best high rate performance.[33] Furthermore, the spherical aggregates morphology should promote the formation of a homogeneous slurry to be casted on the aluminum positive electrode current collector.

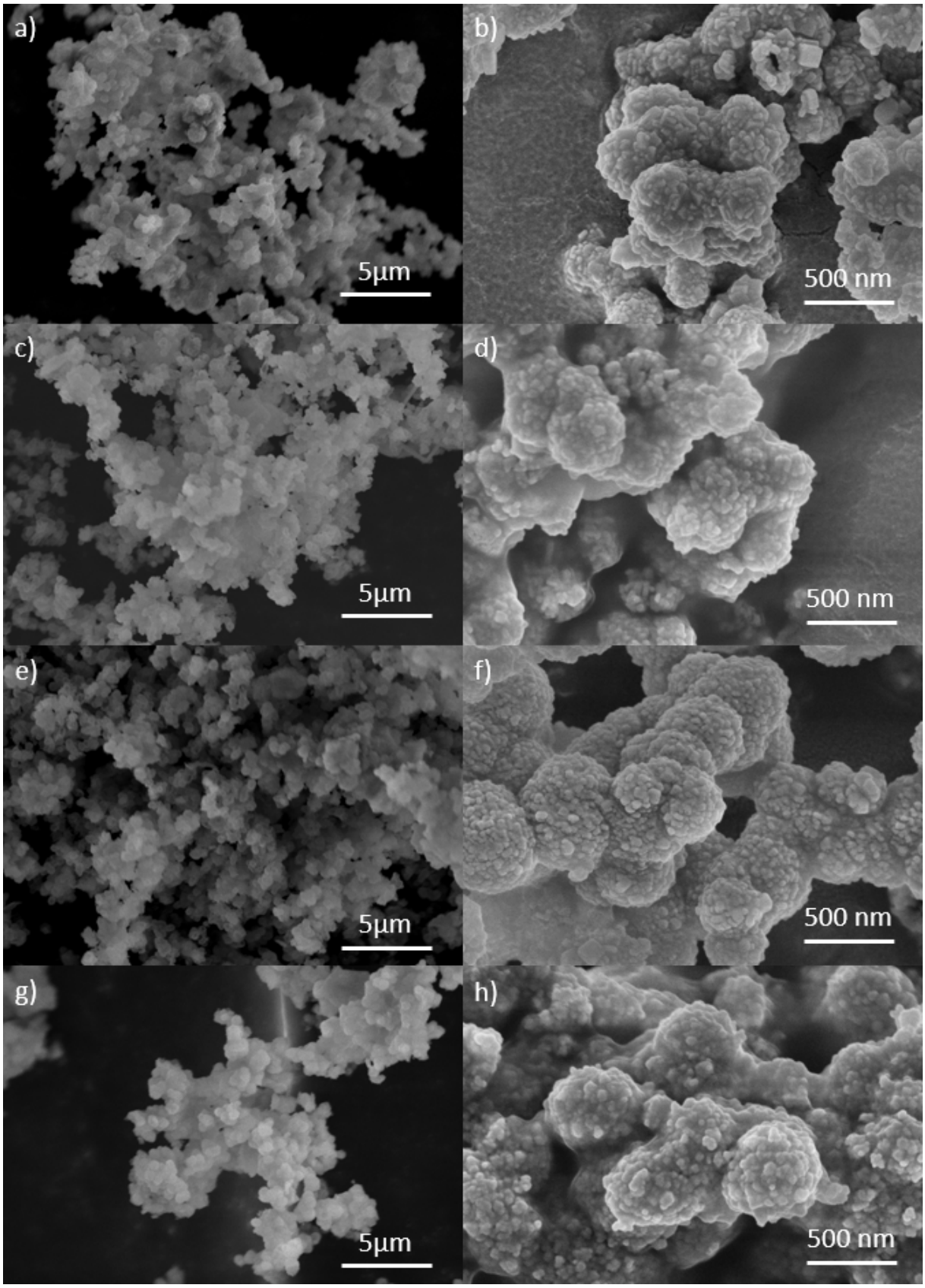

Figure 4: SEM images of a) $NVPFO_{0.80}$, c) $NVPFO_{1.35}$, e) $NVPFO_{1.60}$, and g) $NVPFO_2$. The corresponding SEM-FEG images of b) $NVPFO_{0.80}$, d) $NVPFO_{1.35}$, f) $NVPFO_{1.60}$, and h) $NVPFO_2$.

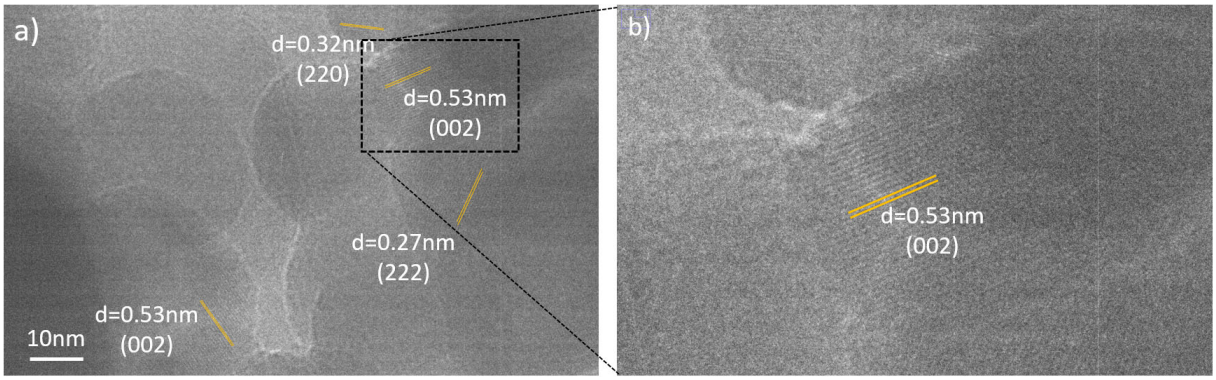

Figure 5. a) and b) HRTEM for $NVPFO_{1.35}$.

The different lattice fringes observed by HRTEM (0.27 nm (222), 0.32 nm (220), 0.53 nm (002) and 0.55 nm (111)) confirm the good crystallinity of the small primary particles of $NVPFO_{1.35}$. Moreover, the observation of various crystalline lattices (**Figure 5**) suggests the absence of preferential orientation and may weight in favor of crystallite's spherical shape. Similar results are obtained for the rest of the $NVPFO_y$ series and are presented in **Figure S9**.

3.2 Transport and Electrochemical properties

Thus, this $NVPFO_y$ series of compounds presenting different chemical compositions while preserving a very similar particle's size and morphology represents an ideal case to study the effect of the oxygen content on the transport properties. A first analysis of the complex impedance data of the $NVPFO_y$ compounds reveals quite similar electrical behavior in all studied samples. **Figure 6** depicts complex impedance plots for each compound recorded at 200 °C. Here, the complex impedance data (Z*) have already been normalized regarding the shape factor (l/A, thickness over area) of each sample according to the relation $Z_s^* = Z^*.A/l$, given rise to the specific impedance (Z_s^*). This approach allows to compare the samples directly and their overall electrical resistivity can be promptly read at the low-frequency intercept of the impedance data on the axis representing the real part of specific impedance (Z_s').[44] A common feature in the electrical behavior is the distorted semi-circles probably caused by a jointly contribution of grains and grain boundaries at high and middle-frequency ranges, respectively.[28,45] The deconvolution of these contributions applying a suitable equivalent circuit to fit the impedance data unveils that the grain impedance response is about one order of magnitude higher than that of the grain boundaries (**Figure S10**).[28] However, the deconvolution procedure is not possible for all samples nor all temperatures of measurements due to the very similar electrical relaxation processes of grains and grain boundaries. In this case, only the overall impedance of the samples can be determined but it should be mostly controlled by the

impedance of the grains (**Figure S10**). As shown in **Figure 6**, $NVPFO_{1.35}$ compound presents the highest conductivity among the $NVPFO_y$ compounds investigated. Another similar aspect in the impedance response obtained at 200 ºC for this series, is the absence of polarization phenomenon (ion-blocking effect) characterized by a steep increase of the imaginary part of impedance (Z_s") at low-frequency range, which is the main signature of an ionic conductor.[46,47] Therefore, it is reasonable to assume that the nanometric $NVPFO_y$ compounds investigated here are mostly electronic conductors at this temperature (200 ºC).

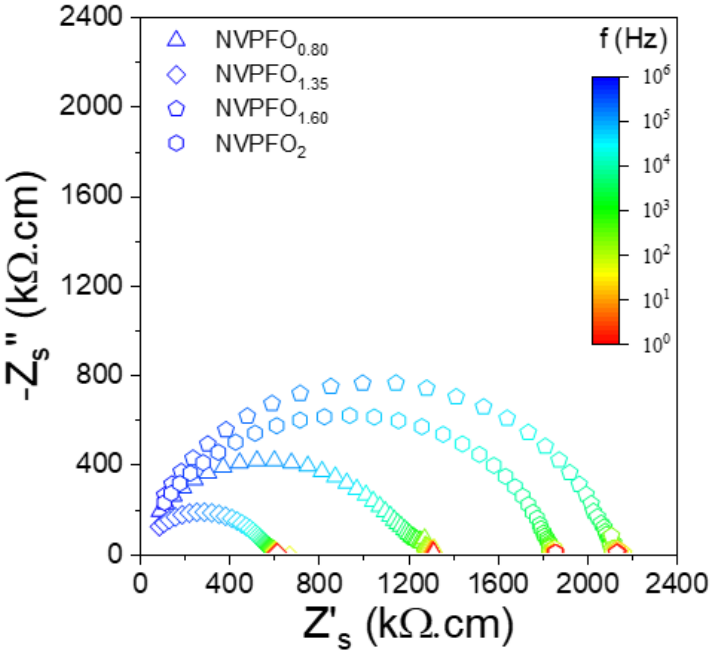

Figure 6: EIS analyses of the $Na_3V_2(PO_4)_2F_{3-y}O_y$ compounds performed at 200ºC, namely, $NVPFO_{0.80}$, $NVPFO_{1.35}$, $NVPFO_{1.60}$ and $NVPFO_2$. The complex impedance data shown here have already been normalized regarding the shape factor of each sample for comparison purposes.

However, when the electrical behavior of these compounds is analyzed as function of the temperature, a more intricate impedance behavior is unfolded. **Figure 7** displays the dependence on frequency of the real (Z_s') and imaginary (-Z_s") parts of the specific impedance of the series of materials in the whole range of temperatures investigated (100-300°C). Again, the electrical resistivity can be promptly read on the left *y* axis at the low frequency plateau because the impedance data have been normalized by the shape factor of each sample. With respect to the imaginary part of impedance, the -Z_s" peak shifts to higher frequencies as the temperature is increased. This behavior is due to the drop in the electrical resistivity with the temperature which increases the relaxation frequency (f) of the semicircle that is inversely proportional to the resistance (R) and capacitance (C) of the sample ($f \sim 1/RC$).[44] Although in the middle-frequency range (10-100Hz), interferences of the electrical wiring in the measurement room increases the dispersion of measurements, the overall trend of evolution is

not influenced. Nonetheless, the most important feature that differs the samples is spotted at low-frequency range (1-10 Hz), where the polarization phenomenon should arise.[46,47] $NVPFO_{0.80}$ (**Figure 7a**) and $NVPFO_{1.35}$ (**Figure 7b**) samples present a typical behavior of an electronic conductor, since from the high-frequency -Z_s" peak, the imaginary part, diminishes continuously with the decrease on frequency, for all temperatures. No polarization is observed, as expected if the main charge carriers in the sample are electrons, when the electrodes used in the measurement (gold in this case) present electronic conductivity several orders of magnitude higher than the analyzed sample. On the other hand, $NVPFO_{1.60}$ (**Figure 7c**) and $NVPFO_2$ (**Figure 7d**) samples exhibit at high temperatures an increasing of -Z_s" in the low-frequency range, evidencing a polarization behavior. This feature is typical for an ion conductor, and it is caused by the blockage of mobile ions in the metallic electrodes. Therefore, at high temperatures (> 180ºC) the ionic contribution on overall conductivity for these two samples is likely to be as important as the electronic one.[46,47]

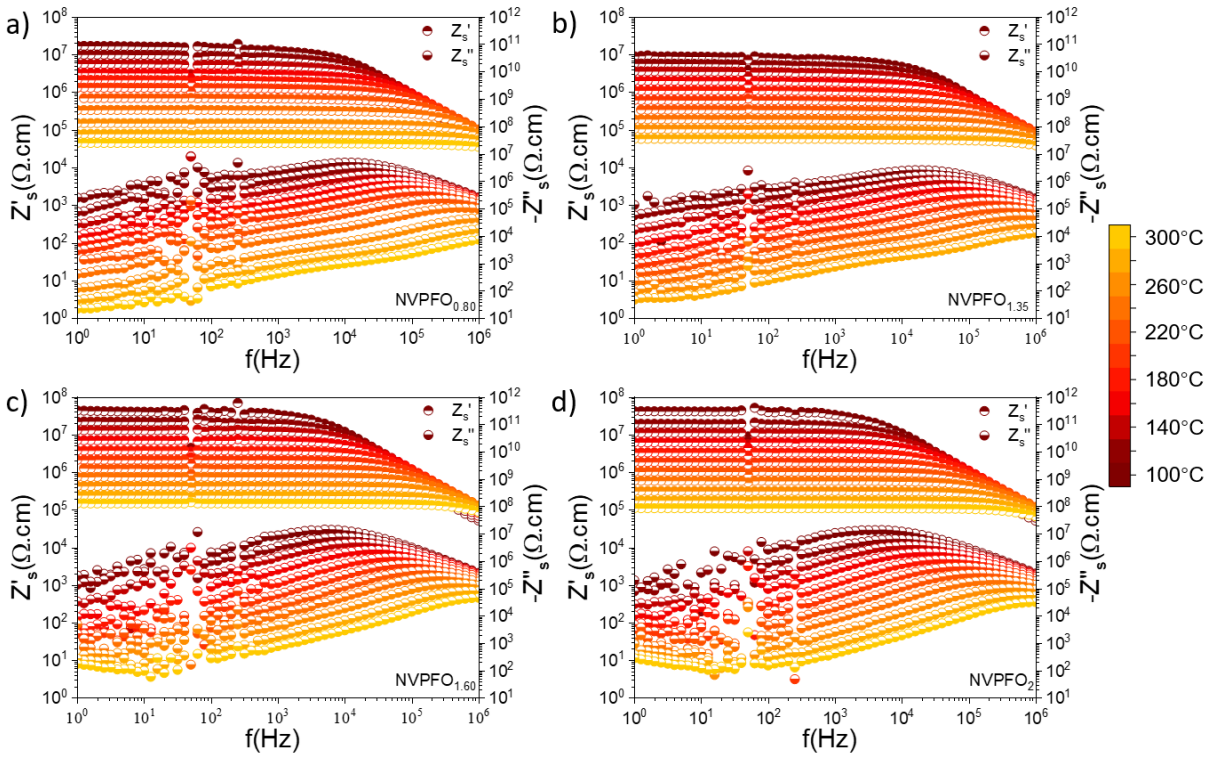

Figure 7: Dependence on frequency of the real (half up filled symbol) and imaginary (half down filled symbol) parts of impedance of the a) $NVPFO_{0.80}$, b) $NVPFO_{1.35}$, c) $NVPFO_{1.60}$ and d) $NVPFO_2$ samples. The real and imaginary parts of impedance have already been normalized regarding the shape factor of the samples.

Finally, the electrical conductivity dependence on the inverse of temperature (**Figure 8**) is plotted applying the linearized form of the Arrhenius-like relation (Eq. 1), which is mostly used for ionic conductors but sometimes also applied for electronic conductors.[47–49]

$$\sigma T = \sigma_0 \exp\left(\frac{-E_a}{k_B T}\right) \quad (1)$$

Here, σ_0 is the pre-exponential factor, E_a is the activation energy for ionic conductivity, k_B is the Boltzmann constant, and T is the absolute temperature. Following this methodology, the linear fit slope is proportional to the activation energy, which therefore provides access to the energetic barrier of the mechanism responsible for the electrical transport.[49] **Figure 8** exhibits the Arrhenius-like plots of the overall electrical conductivity of the $NVPFO_y$ compounds investigated in this work as well as those reported in literature by Broux et al..[28] Overall, the dependence of the electrical conductivity on temperature for the nanometric $NVPFO_y$ compounds seems to present a low (T<180ºC) and a high (T>180ºC) temperature regime due to the dominating electronic transport at low temperatures and the mixed ionic-electronic conducting behavior at higher temperatures. The activation energy of the high temperature regime is considerably higher than the low-temperature one for all nanometric $NVPFO_y$ samples (**Table 4**). However, when the samples are compared at the same temperature regime, the activation energy of nanometric $NVPFO_y$ samples are nearly the same if uncertainties are considered (**Table 4**). Even though, the $NVPFO_{1.35}$ sample presents the highest overall conductivity in the entire investigated temperature range. Two activation energy regimes have been also visualized for the micrometric $NVPFO_y$ compounds reported in literature.[25] Nevertheless, the transition on this last case takes place around the temperature of 130 ºC and it has been attributed to a structural change induced by a mobility of the Na^+ ions on a ring. Besides, in the low temperature regime, the micrometric $NVPFO_y$ compounds reported in literature show much lower conductivity and higher activation energy than the nanometric $NVPFO_y$ compounds studied in this work (**Table 4**).[28] Indeed, $NVPFO_{1.35}$ possess, at 100 °C, an electrical conductivity nearly two order of magnitude higher than the micrometric $NVPFO_y$ reported in the literature, which clearly demonstrates the advantage of particle's downsizing to improve electrical transport. Besides, these micrometric $NVPFO_y$ compounds were mostly ionic conductors on the contrast with the nanometric compounds of this investigation. Nonetheless, the high temperature polarization phenomenon spotted in the impedance response of samples $NVPFO_{1.60}$ (**Figure 7c**) and $NVPFO_2$ (**Figure 7d**) is in good agreement with the literature data, once above 180 ºC the ionic conductivity of the micrometric compounds is in the same order of magnitude of the electronic conductivity of the nanometric compounds reported here. As a final point, $NVPFO_{1.35}$ and $NVPFO_{0.80}$ exhibit the best electrical conductivities within the investigated series. Besides the fact that V^{3+}/V^{4+} bi-octahedra does not form continuous chains throughout the structure, which probably hinder the electronic transport,

the decreasing of the particles size to nanometric scale are likely to created additional energy levels on the band gap of these compounds due to surface disorder, fostering the electronic transport. After the high temperature impedance measurement, the $NVPFO_{1.35}$ was characterized again with XRD to check for its structure. The invariant peaks' position confirms that the material retains its original crystal structure (**Figure S11**).

Table 4: Activation energy for all the materials with temperature dividing point at ~ 180°C for nanometric $NVPFO_y$ (y = 0.8, 1.35, 1.6 and 2) and at ~130°C for micrometric NVPFOy (y = 1 and 0)[28].

Samples		$NVPFO_2$	$NVPFO_{1.60}$	$NVPFO_{1.35}$	$NVPFO_{0.80}$	$NVPFO_1$	$NVPFO_0$
Activation Energy (eV)	Low-T	0.43(3)	0.43(3)	0.42(3)	0.42(1)	0.87(1)	0.97(5)
	High-T	0.69(2)	0.65(2)	0.69(2)	0.79(4)	0.69(1)	0.77(1)

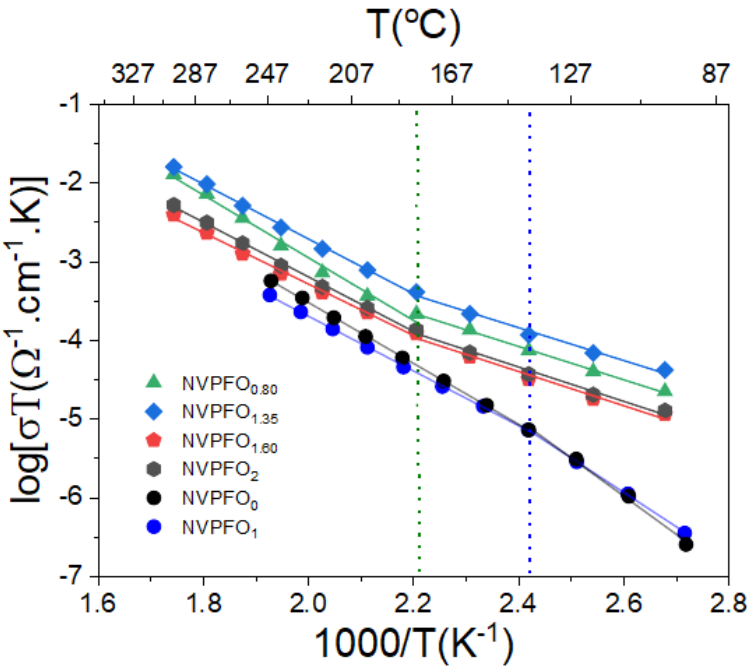

Figure 8: Arrhenius-like plots of the dependence of the overall electrical conductivity of $NVPFO_y$ compounds on the inverse temperature. Black and deep blue points correspond to literature data for $Na_3V_2(PO_4)_2F_3$ and $Na_3V_2(PO_4)_2F_2O$ sintered samples of micrometric grain size, respectively[28].

Figures 9a-d demonstrate the Galvanostatic charge and discharge curves profiles of the 1st ,2nd, and 5th cycles obtained at C/20 in the potential range 2.5-4.3 V vs. Na^+/Na. The four electrode materials present two "pseudo-plateaus" of equivalent length characteristic of the $NVPFO_y$ family[7,8,37,50] and a very low polarization indicating a good diffusion process of Na^+ ions within the materials and the electrodes. All of them exhibit a first charge capacity of 126 $mAh.g^{-1}$ indicating the extraction of two Na^+ (the theoretical capacity for $NVPFO_2$ is 130 $mAh.g^{-1}$) and show comparable first cycle irreversible capacity losses, leading thus to similar reversible capacities around 114 $mA.h.g^{-1}$. As it could be expected from the mixed V^{3+}/V^{4+} initial

composition, the electrochemical curves of $NVPFO_{0.80,}$ $NVPFO_{1.35}$ and $NVPFO_{1.60}$ are composed by two rather slopping "plateaus" indicating that the Na^+ intercalation/de-intercalation is mainly driven by monophasic reaction.[30] On the other hand, $NVPFO_2$ exhibits more horizontal plateaus that suggests the presence of biphasic reaction upon the reversible desodiation.[51] These different reaction mechanisms are supported by the corresponding first derivative curves presented in **Figure 9e** which reveals intense and narrow peaks for $NVPFO_2$ versus rather broad and less defined peaks for the other members of the series.[25] From a practical point of view, the solid solution reaction usually leads to a smoother potential jump between the two pseudo-plateaus and could attenuate the heat generated due to the phase transition that is detrimental to long-term cycling.[51,52] Meanwhile, it could be observed that the average redox potential of the second pseudo-plateau tends to rise with the increase of fluorine content due to the more ionic character of V-F bond compared to V=O one (**Figure 9e**). On the other hand,

the average oxidation potential for the lower voltage plateau is less affected by composition and could not be linked to the fluorine content (**Figure9e**).

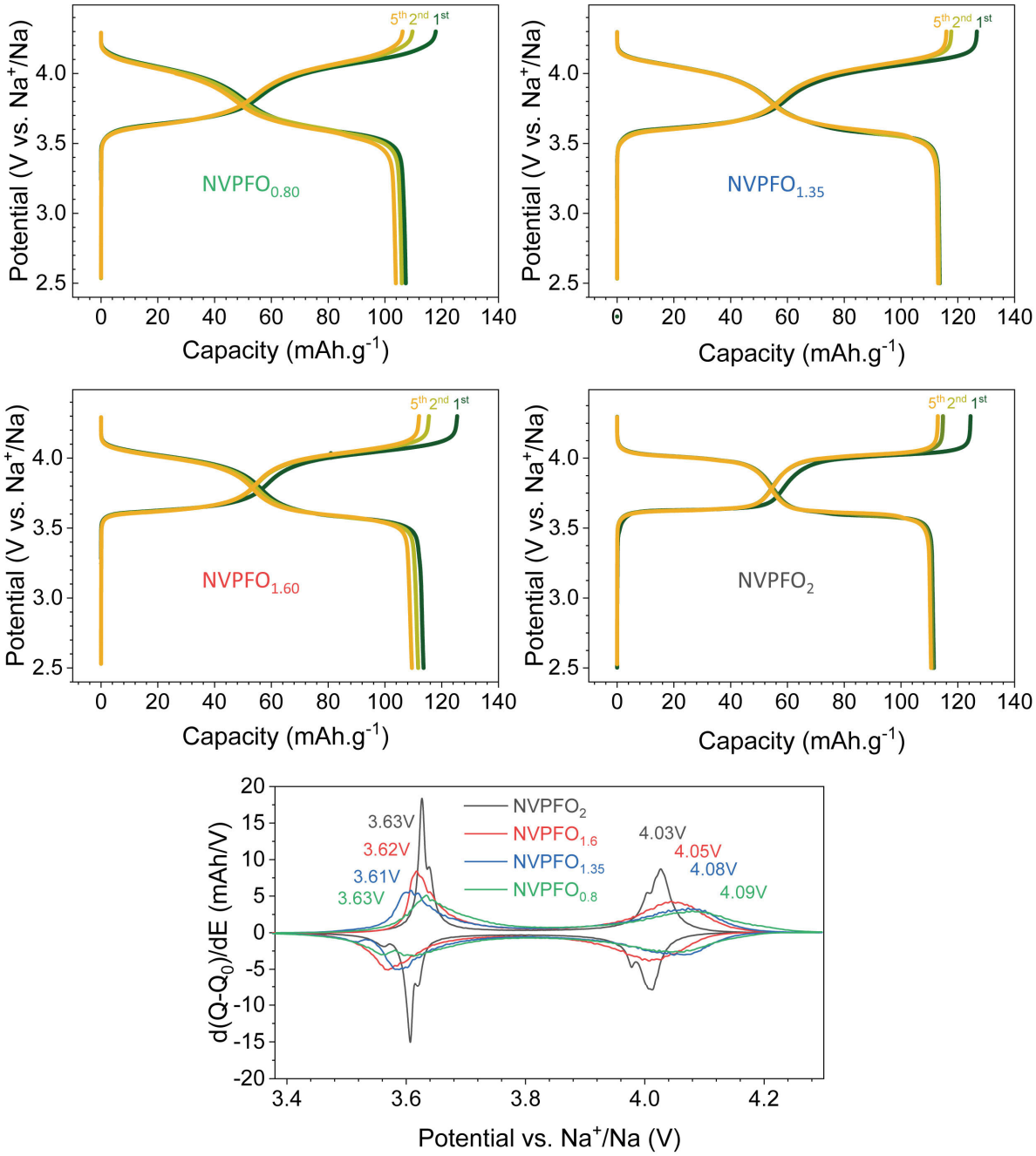

Figure 9: a-d) Galvanostatic charge and discharge curves obtained in half-cell for all the $NVPFO_y$ electrode materials at the cycling rate of C/20. All the electrodes were prepared with 88 wt.% of active materials, 7 wt.% of carbon black, and 5 wt.% of PVDF in order to better observe the effect of composition change of $NVPFO_y$. e) First derivative curves corresponding to the 5th cycle performed at C/20.

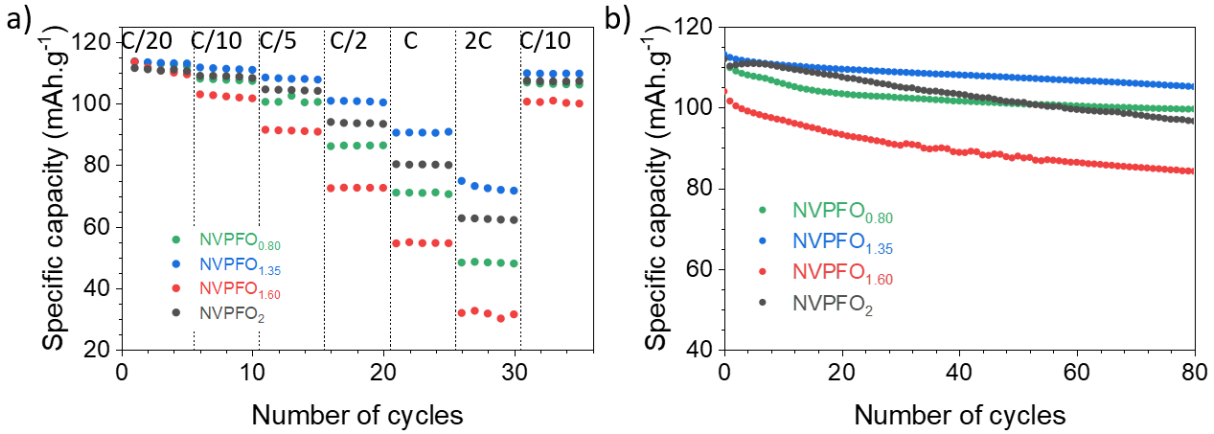

Figure 10: a) Specific (reversible) capacities obtained for all the studied electrode materials at various C-rates from C/20 to 2C. b) Long term cycling performance of all the $NVPFO_y$ materials prepared without any carbon coating at C/10. It represents cycling time between 1200 and 1500 hours depending on the electrode materials.

Although at low current densities all the electrode materials could nearly reach their theoretical capacities, the capacity retention differs within the series when the charges/discharges become faster (**Figure 10a** and **Figure S12**). For example, $NVPFO_{1.35}$ exhibits ~90 mAh.g^{-1} at 1C while only 80 mAh.g^{-1}, 70 mAh.g^{-1} and 50 mAh.g^{-1} are measured for $NVPFO_2$, $NVPFO_{0.80}$ and $NVPFO_{1.60}$ respectively. There is no straightforward trend between the rate performance and the oxygen content within the series, however, as for the transport properties it can be noticed that $Na_3V^{3+}_{0.65}V^{4+}_{1.35}(PO_4)_2F_{1.65}O_{1.35}$ exhibits the best results and $Na_3V^{3+}_{0.40}V^{4+}_{1.60}(PO_4)_2F_{1.40}O_{1.60}$ the worst ones. Nevertheless, a direct correlation between electrical conductivity of the pristine materials and C-rate performances is not possible since the galvanostatic measurements involve Na^+ extraction/insertion and hence, the composition as well as the vanadium mean oxidation state change upon cycling. It is important to notice that after testing the rate performance, the full capacity is recovered at C/10 for all series, which indicates that all the materials reveal good structural stability and the capacity drop at higher current density is only due to kinetic limitations.

As represented **Figure 10b** and **Figure S13**, all the materials exhibit a capacity retention higher than 80% after 80 cycles at C/10 and an initial specific capacity higher than 100 mAh.g^{-1}. Once again, $Na_3V^{3+}_{0.65}V^{4+}_{1.35}(PO_4)_2F_{1.65}O_{1.35}$ demonstrates the best performance with an initial specific capacity of 115 mAh.g^{-1} and a capacity retention rate of 91% after 80 cycles which also confirms the good structural stability upon long-term cycling. Finally, considering the active mass rich formulation and high mass loading of the electrode as well as the absence of carbon-coating, $NVPFO_{1.35}$ with nano-spherical morphology reveals extremely favorable energy storage performance.

Thus, by combining the results obtained in this work with those reported in the literature, the (partial) oxygen for fluorine substitution enhances the transport properties, which leads to better high-rate capacity retentions, and improves the structural stability at overcharged states.[30] Besides, two Na^+ ions can be reversibly extracted for all the $NVPFO_y$ family members thanks to the possibility to access to V^{4+}/V^{3+} and V^{5+}/V^{4+} (or $(V=O)^{3+}/(V=O)^{2+}$) redox couples that are simultaneously activated during the electrochemical de-intercalation.[30,33,36] Moreover, the partial O^{2-} for F^- substitution most probably prevents Na^+/vacancy ordering during charge/discharge, which induces a monophasic Na^+ de-intercalation/re-intercalation upon cycling whereas mainly biphasic behavior is observed for $Na_3V^{3+}_2(PO_4)_2F_3$ and $Na_3V^{4+}_2(PO_4)_2FO_2$.[31] This leads to more sloping charge/discharge curves, lowers the potential jump after the extraction of the first Na^+ ion and hence, probably reduces the heat generation that is detrimental for the cell stability. On the other hand, the average voltage corresponding to Na^+ extraction continuously decreases upon oxygen for fluorine substitution. It decreases from ~ 3.95 V vs Na/Na^+ for NVPF to ~ 3.8 V vs Na/Na^+ for $NVPFO_2$, which consequently decreases the energy density, as the theoretical capacity remains almost constant.[8,30,33] Therefore, it seems that a moderated O^{2-} for F^- substitution ratio would be the best compromise to take the benefit listed above without affecting too much the average potential.

4. Conclusion

To summarize, four compounds that belong to the $Na_3V^{3+}_{2-y}V^{4+}_y(PO_4)_2F_{3-y}O_y$ ($0 < y < 2$) family, and possessing different O^{2-}/F^- ratios ("*y*" parameter), were obtained through a low temperature solvothermal synthesis. They all possess the same nanospherical morphology that represents an ideal series to investigate the impact of the oxygen content (or V^{3+}/V^{4+} initial ratio) on the electronic conductivity as well as on the energy storage performance. The structure of each compound was determined carefully by Rietveld refinement and the O^{2-} content trend was confirmed by Infrared spectroscopy. Besides, Raman spectroscopy is for the first time reported for this series and reveals to be an efficient characterization technique to estimate the oxygen content within the $Na_3V^{3+}_{2-y}V^{4+}_y(PO_4)_2F_{3-y}O_y$ family. This work also shows the great impact of particle downsizing on the electrical conductivity that is improved by more than two order of magnitude compared to their bulk counterpart. Moreover, it was demonstrated that a high amount of mixed V^{3+}/V^{4+} bi-octahedra most probably favors the electronic mobility. In this work, $Na_3V^{3+}_{1.65}V^{4+}_{1.35}(PO_4)_2F_{1.65}O_{1.35}$ (y = 1.35) and $Na_3V^{3+}_{1.20}V^{4+}_{0.80}(PO_4)_2F_{2.20}O_{0.80}$ (y = 0.80) show the lowest electrical resistivity with 9×10^6 Ω.cm and 2×10^7 Ω.cm respectively at 100°C. $Na_3V^{3+}_{1.65}V^{4+}_{1.35}(PO_4)_2F_{1.65}O_{1.35}$ (y = 1.35) also presents the best rate capacity retention

and stability upon long-term cycling. Finally, this study reveals that the intrinsic properties of $NVPFO_y$ materials could be improved by tailoring the oxygen content and mixed V^{3+}/V^{4+} polyanionic electrode material should be further investigated to reach the best energy storage performance.

Supporting Information

Additional XRD patterns and Rietveld refinements; reproducibility of the electrochemical performance; Raman spectra of the $NVPFO_y$ series and of carbon coated NVPF; Statistic of particle size distribution; HRTEM images; Figure representing the deconvolution of grain and grain boundary contributions of complex impedance data; XRD patterns before and after EIS measurements; Galvanostatic Charge/discharge curve at different C-rates; Long term cycling performance and coulombic efficiency.

Acknowledgements

The authors thank the Materials Physics and Chemistry Doctoral School (ED397) of Sorbonne University for the funding as well as the financial support of Région Nouvelle Aquitaine, of the French National Research Agency (STORE-EX Labex Project ANR-10-LABX-76-01) and of the European Union's Horizon 2020 research and innovation program under grant agreement No 875629 (NAIMA project).

References

(1) European Climate Law | Climate Action.

(2) Hu, Y. S.; Komaba, S.; Forsyth, M.; Johnson, C.; Rojo, T. A New Emerging Technology: Na-Ion Batteries. *Small Methods* **2019**, *3* (4), 2–3. https://doi.org/10.1002/smtd.201900184.

(3) Hasa, I.; Mariyappan, S.; Saurel, D.; Adelhelm, P.; Koposov, A. Y.; Masquelier, C.; Croguennec, L.; Casas-Cabanas, M. Challenges of Today for Na-Based Batteries of the Future: From Materials to Cell Metrics. *J. Power Sources* **2021**, *482* (September 2020), 228872. https://doi.org/10.1016/j.jpowsour.2020.228872.

(4) Tarascon, J. M. Na-Ion versus Li-Ion Batteries: Complementarity Rather than Competitiveness. *Joule* **2020**, *4* (8), 1616–1620. https://doi.org/10.1016/j.joule.2020.06.003.

(5) Broux, T.; Fauth, F.; Hall, N.; Chatillon, Y.; Bianchini, M.; Bamine, T.; Leriche, J. B.; Suard, E.; Carlier, D.; Reynier, Y.; Simonin, L.; Masquelier, C.; Croguennec, L. High Rate Performance for Carbon-Coated Na3V2(PO4)2F3 in Na-Ion Batteries. *Small Methods* **2019**, *3* (4), 1–12. https://doi.org/10.1002/smtd.201800215.

(6) Yan, G.; Dugas, R.; Tarascon, J.-M. The Na3V2(PO4)2F3/Carbon Na-Ion Battery: Its Performance Understanding as Deduced from Differential Voltage Analysis. *J. Electrochem. Soc.* **2018**, *165* (2), A220–A227. https://doi.org/10.1149/2.0831802jes.

(7) Bianchini, M.; Xiao, P.; Wang, Y.; Ceder, G. Additional Sodium Insertion into Polyanionic Cathodes for Higher-Energy Na-Ion Batteries. *Adv. Energy Mater.* **2017**, *7* (18), 1700514. https://doi.org/10.1002/aenm.201700514.

(8) Park, Y. U.; Seo, D. H.; Kim, H.; Kim, J.; Lee, S.; Kim, B.; Kang, K. A Family of High-Performance Cathode Materials for Na-Ion Batteries, Na3(VO1-XPO4)2 F1+2x ($0 \leq x \leq 1$): Combined First-Principles and Experimental Study. *Adv. Funct. Mater.* **2014**, *24* (29), 4603–4614. https://doi.org/10.1002/adfm.201400561.

(9) Bianchini, M.; Brisset, N.; Fauth, F.; Weill, F.; Elkaim, E.; Suard, E.; Masquelier, C.; Croguennec, L. Na3V2(PO4)2F3 Revisited: A High-Resolution Diffraction Study. *Chem. Mater.* **2014**, *26* (14), 4238–4247. https://doi.org/10.1021/cm501644g.

(10) Zhu, Y.; Xu, E.; Zhang, J.; Quan, J.; Wang, H.; Sun, Z.; Jiang, Y. Fabrication of a Sandwiched Core Carbon Sphere@Na3V2(PO4)2O2F@N-Doped Carbon Cathode for Superior Sodium-Ion Batteries. *ACS Appl. Energy Mater.* **2021**, *4* (4), 3952–3961. https://doi.org/10.1021/acsaem.1c00334.

(11) Li, L.; Liu, X.; Tang, L.; Liu, H.; Wang, Y. G. Improved Electrochemical Performance of High Voltage Cathode Na 3 V 2 (PO 4) 2 F 3 for Na-Ion Batteries through Potassium Doping. *J. Alloys Compd.* **2019**, *2*, 203–211. https://doi.org/10.1016/j.jallcom.2019.03.127.

(12) Li, H.; Zhang, X.; Zhao, Z.; Hu, Z.; Liu, X.; Yu, G. Flexible Sodium-Ion Based Energy Storage Devices: Recent Progress and Challenges. *Energy Storage Mater.* **2020**, *26* (August 2019), 83–104. https://doi.org/10.1016/j.ensm.2019.12.037.

(13) Shen, C.; Long, H.; Wang, G.; Lu, W.; Shao, L.; Xie, K. Na3V2(PO4)2F3@C Dispersed within Carbon Nanotube Frameworks as a High Tap Density Cathode for High-Performance Sodium-Ion Batteries. *J. Mater. Chem. A* **2018**, *6* (14), 6007–6014.

https://doi.org/10.1039/c8ta00990b.

(14) Li, F.; Zhao, Y.; Xia, L.; Yang, Z.; Wei, J.; Zhou, Z. Well-Dispersed Na3V2(PO4)2F3@rGO with Improved Kinetics for High-Power Sodium-Ion Batteries. *J. Mater. Chem. A* **2020**, *8* (25), 12391–12397. https://doi.org/10.1039/d0ta00130a.

(15) Jin, H.; Dong, J.; Uchaker, E.; Zhang, Q.; Zhou, X.; Hou, S.; Li, J.; Cao, G. Three Dimensional Architecture of Carbon Wrapped Multilayer Na3V2O2(PO4)2F Nanocubes Embedded in Graphene for Improved Sodium Ion Batteries. *J. Mater. Chem. A* **2015**, *3* (34), 17563–17568. https://doi.org/10.1039/c5ta03164h.

(16) Xun, J.; Zhang, Y.; Xu, H. One Step Synthesis of Vesicular Na3V2(PO4)2F3 and Network of Na3V2(PO4)2F3@graphene Nanosheets with Improved Electrochemical Performance as Cathode Material for Sodium Ion Battery. *Inorg. Chem. Commun.* **2020**, *115*, 107884. https://doi.org/10.1016/j.inoche.2020.107884.

(17) Bi, L.; Miao, Z.; Li, X.; Song, Z.; Zheng, Q.; Lin, D. Improving Electrochemical Performance of Na3(VPO4)2O2F Cathode Materials for Sodium Ion Batteries by Constructing Conductive Scaffold. *Electrochim. Acta* **2020**, *337*, 135816. https://doi.org/10.1016/j.electacta.2020.135816.

(18) Wang, T.; Zhang, W.; Li, H.; Hu, J.; Lai, Y.; Zhang, Z. N-Doped Carbon Nanotubes Decorated Na 3 V 2 (PO 4) 2 F 3 as a Durable Ultrahigh-Rate Cathode for Sodium Ion Batteries. *ACS Appl. Energy Mater.* **2020**, *3* (4), 3845–3853. https://doi.org/10.1021/acsaem.0c00283.

(19) Olchowka, J.; Nguyen, L. H. B.; Broux, T.; Sanz Camacho, P.; Petit, E.; Fauth, F.; Carlier, D.; Masquelier, C.; Croguennec, L. Aluminum Substitution for Vanadium in the Na3V2(PO4)2F3 and Na3V2(PO4)2FO2 Type Materials. *Chem. Commun.* **2019**, *55* (78), 11719–11722. https://doi.org/10.1039/c9cc05137f.

(20) Nguyen, L. H. B.; Olchowka, J.; Belin, S.; Sanz Camacho, P.; Duttine, M.; Iadecola, A.; Fauth, F.; Carlier, D.; Masquelier, C.; Croguennec, L. Monitoring the Crystal Structure and the Electrochemical Properties of Na3(VO)2(PO4)2F through Fe3+ Substitution. *ACS Appl. Mater. Interfaces* **2019**, *11* (42), 38808–38818. https://doi.org/10.1021/acsami.9b14249.

(21) Iarchuk, A. R.; Sheptyakov, D. V; Abakumov, A. M. Hydrothermal Microwave-Assisted Synthesis of Na 3+ x V 2– y Mn y (PO 4) 2 F 3 Solid Solutions as Potential Positive

Electrodes for Na-Ion Batteries. *ACS Appl. Energy Mater.* **2021**, *4* (5), 5007–5014. https://doi.org/10.1021/acsaem.1c00579.

(22) Liu, W.; Yi, H.; Zheng, Q.; Li, X.; Zhang, H. Y-Doped Na3V2(PO4)2F3 Compounds for Sodium Ion Battery Cathodes: Electrochemical Performance and Analysis of Kinetic Properties. *J. Mater. Chem. A* **2017**, *5* (22), 10928–10935. https://doi.org/10.1039/C7TA03133E.

(23) Shen, X.; Zhao, J.; Li, Y.; Sun, X.; Yang, C.; Liu, H.; Hu, Y. S. Controlled Synthesis of Na3(VOPO4)2F Cathodes with an Ultralong Cycling Performance. *ACS Appl. Energy Mater.* **2019**, *2* (10), 7474–7482. https://doi.org/10.1021/acsaem.9b01458.

(24) Cai, Y.; Cao, X.; Luo, Z.; Fang, G.; Liu, F.; Zhou, J.; Pan, A.; Liang, S. Caging Na3V2(PO4)2F3 Microcubes in Cross-Linked Graphene Enabling Ultrafast Sodium Storage and Long-Term Cycling. *Adv. Sci.* **2018**, *2*, 1800680. https://doi.org/10.1002/advs.201800680.

(25) Olchowka, J.; Nguyen, L. H. B.; Petit, E.; Camacho, P. S.; Masquelier, C.; Carlier, D.; Croguennec, L. Ionothermal Synthesis of Polyanionic Electrode Material Na3V2(PO4)2FO2 through a Topotactic Reaction. *Inorg. Chem.* **2020**, *59* (23), 17282–17290. https://doi.org/10.1021/acs.inorgchem.0c02546.

(26) Qi, Y.; Zhao, J.; Yang, C.; Liu, H.; Hu, Y. S. Comprehensive Studies on the Hydrothermal Strategy for the Synthesis of Na3(VO1−xPO4)2F1+2x ($0 \leq x \leq 1$) and Their Na-Storage Performance. *Small Methods* **2019**, *3* (4), 1800111. https://doi.org/10.1002/smtd.201800111.

(27) Xu, J.; Chen, J.; Tao, L.; Tian, Z.; Zhou, S.; Zhao, N.; Wong, C. Investigation of Na3V2(PO4)2O2F as a Sodium Ion Battery Cathode Material: Influences of Morphology and Voltage Window. *Nano Energy* **2019**, *60*, 510–519. https://doi.org/10.1016/j.nanoen.2019.03.063.

(28) Broux, T.; Fleutot, B.; David, R.; Brüll, A.; Veber, P.; Fauth, F.; Courty, M.; Croguennec, L.; Masquelier, C. Temperature Dependence of Structural and Transport Properties for Na3V2(PO4)2F3 and Na3V2(PO4)2F2.5O0.5. *Chem. Mater.* **2018**, *30* (2), 358–365. https://doi.org/10.1021/acs.chemmater.7b03529.

(29) Park, Y. U.; Seo, D. H.; Kwon, H. S.; Kim, B.; Kim, J.; Kim, H.; Kim, I.; Yoo, H. I.; Kang, K. A New High-Energy Cathode for a Na-Ion Battery with Ultrahigh Stability. *J.*

Am. Chem. Soc. **2013**, *135* (37), 13870–13878. https://doi.org/10.1021/ja406016j.

(30) Nguyen, L. H. B.; Broux, T.; Camacho, P. S.; Denux, D.; Bourgeois, L.; Belin, S.; Iadecola, A.; Fauth, F.; Carlier, D.; Olchowka, J.; Masquelier, C.; Croguennec, L. Stability in Water and Electrochemical Properties of the Na3V2(PO4)2F3 – Na3(VO)2(PO4)2F Solid Solution. *Energy Storage Mater.* **2019**, *20* (April), 324–334. https://doi.org/10.1016/j.ensm.2019.04.010.

(31) Dacek, S. T.; Richards, W. D.; Kitchaev, D. A.; Ceder, G. Structure and Dynamics of Fluorophosphate Na-Ion Battery Cathodes. *Chem. Mater.* **2016**, *28* (15), 5450–5460. https://doi.org/10.1021/acs.chemmater.6b01989.

(32) Qi, Y.; Mu, L.; Zhao, J.; Hu, Y. S.; Liu, H.; Dai, S. Superior Na-Storage Performance of Low-Temperature-Synthesized Na3(VO1-XPO4)2F1+2x (0≤x≤1) Nanoparticles for Na-Ion Batteries. *Angew. Chemie - Int. Ed.* **2015**, *54* (34), 9911–9916. https://doi.org/10.1002/anie.201503188.

(33) Fang, R.; Olchowka, J.; Pablos, C.; Camacho, P. S.; Carlier, D.; Croguennec, L.; Cassaignon, S. Effect of the Particles Morphology on the Electrochemical Performance of Na3V2(PO4)2F3-yOy. *Batter. Supercaps* **2021**. https://doi.org/10.1002/batt.202100179.

(34) Rodríguez-Carvajal, J. Recent Advances in Magnetic Structure Determination by Neutron Powder Diffraction. *Phys. B Condens. Matter* **1993**, *192* (1–2), 55–69. https://doi.org/10.1016/0921-4526(93)90108-I.

(35) Le Meins, J.-M.; Crosnier-Lopez, M.-P.; Hemon-Ribaud, A.; Courbion, G. Phase Transitions in the Na3M2(PO4)2F3 Family (M=Al3+, V3+, Cr3+, Fe3+, Ga3+): Synthesis, Thermal, Structural, and Magnetic Studies. *J. Solid State Chem.* **1999**, *148* (2), 260–277. https://doi.org/10.1006/jssc.1999.8447.

(36) Nguyen, L. H. B.; Iadecola, A.; Belin, S.; Olchowka, J.; Masquelier, C.; Carlier, D.; Croguennec, L. A Combined Operando Synchrotron X-Ray Absorption Spectroscopy and First-Principles Density Functional Theory Study to Unravel the Vanadium Redox Paradox in the Na 3 V 2 (PO 4) 2 F 3 –Na 3 V 2 (PO 4) 2 FO 2 Compositions. *J. Phys. Chem. C* **2020**, *124* (43), 23511–23522. https://doi.org/10.1021/acs.jpcc.0c06967.

(37) Serras, P.; Palomares, V.; Alonso, J.; Sharma, N.; López Del Amo, J. M.; Kubiak, P.; Fdez-Gubieda, M. L.; Rojo, T. Electrochemical Na Extraction/Insertion of Na3V

2O2x(PO4)2F3-2 X. *Chem. Mater.* **2013**, *25* (24), 4917–4925. https://doi.org/10.1021/cm403679b.

(38) Kumar, P. R.; Kubota, K.; Miura, Y.; Ohara, M.; Gotoh, K.; Komaba, S. Na3V2O2(PO4)2F3-2 as a Stable Positive Electrode for Potassium-Ion Batteries. *J. Power Sources* **2021**, *493* (March), 229676. https://doi.org/10.1016/j.jpowsour.2021.229676.

(39) Semykina, D.; Podgornova, O.; Kosova, N. Comparative Study of Na3V2Ox(PO4)2F3-x Prepared via Solid-State and Hydrothermal Synthesis. *Mater. Today Proc.* **2020**, *25*, 497–500. https://doi.org/10.1016/j.matpr.2019.12.368.

(40) Baddour-Hadjean, R.; Pereira-Ramos, J. P. Raman Microspectrometry Applied to the Study of Electrode Materials for Lithium Batteries. *Chem. Rev.* **2010**, *110* (3), 1278–1319. https://doi.org/10.1021/cr800344k.

(41) Criado, A.; Lavela, P.; Ortiz, G.; Tirado, J. L.; Pérez-Vicente, C.; Bahrou, N.; Edfouf, Z. Highly Dispersed Oleic-Induced Nanometric C@Na3V2(PO4)2F3 Composites for Efficient Na-Ion Batteries. *Electrochim. Acta* **2020**, *332*, 135502. https://doi.org/10.1016/j.electacta.2019.135502.

(42) Hardcastle, F. D.; Wachs, I. E. Determination of Vanadium-Oxygen Bond Distances and Bond Orders by Raman Spectroscopy. *J. Phys. Chem.* **1991**, *95* (13), 5031–5041. https://doi.org/10.1021/j100166a025.

(43) Antony, C. J.; Aatiq, A.; Panicker, C. Y.; Bushiri, M. J.; Varghese, H. T.; Manojkumar, T. K. FT-IR and FT-Raman Study of Nasicon Type Phosphates, ASnFe(PO 4)3 [A = Na2, Ca, Cd]. *Spectrochim. Acta - Part A Mol. Biomol. Spectrosc.* **2011**, *78* (1), 415–419. https://doi.org/10.1016/j.saa.2010.11.003.

(44) Cassar, D. R.; Lancelotti, R. F.; Nuernberg, R.; Nascimento, M. L. F.; Rodrigues, A. M.; Diz, L. T.; Zanotto, E. D. Elemental and Cooperative Diffusion in a Liquid, Supercooled Liquid and Glass Resolved. *J. Chem. Phys.* **2017**, *147* (1), 014501. https://doi.org/10.1063/1.4986507.

(45) Montedo, O. R. K.; Nuernberg, R. B.; Piva, R. H.; Jiusti, J.; Arcaro, S.; Piva, D. H. Effect of the Crystalline Layer on the Electrical Behaviour of 17.7Li2O·5.2ZrO2·68.1SiO2·9.0Al2O3 Glass Ceramic Monoliths. *Ceram. Int.* **2021**, *47* (15), 21358–21366. https://doi.org/10.1016/j.ceramint.2021.04.144.

(46) Nuernberg, R. B.; Machado, N. M. P.; Malki, M.; Neyret, M. Electrical Behavior of RuO2-Glass Composites: The Effect of RuO2 Particle Size on the Percolation Threshold. *J. Nucl. Mater.* **2021**, *546*, 152777. https://doi.org/10.1016/j.jnucmat.2020.152777.

(47) Ungureanu, M. C.; Lévy, M.; Souquet, J. L. Mixed Conductivity of Glasses in the P 2 O 5 -V 2 O 5 -Na 2 O System. *Ionics (Kiel).* **1998**, *4* (3), 200–206. https://doi.org/10.1007/BF02375946.

(48) Souquet, J.-L. Ionic and Electronic Transport. In *Encyclopedia of Glass Science, Technology, History, and Culture*; John Wiley & Sons, Ltd, 2021; pp 453–463. https://doi.org/10.1002/9781118801017.ch4.2.

(49) Nuernberg, R. B. Numerical Comparison of Usual Arrhenius-Type Equations for Modeling Ionic Transport in Solids. *Ionics (Kiel).* **2020**, *26* (5), 2405–2412. https://doi.org/10.1007/s11581-019-03243-7.

(50) Broux, T.; Bamine, T.; Fauth, F.; Simonelli, L.; Olszewski, W.; Marini, C.; Ménétrier, M.; Carlier, D.; Masquelier, C.; Croguennec, L. Strong Impact of the Oxygen Content in Na3V2(PO4)2F3-YOy ($0 \leq y \leq 2$) on Its Structural and Electrochemical Properties. *Chem. Mater.* **2016**, *28* (21), 7683–7692. https://doi.org/10.1021/acs.chemmater.6b02659.

(51) Sharma, N.; Serras, P.; Palomares, V.; Brand, H. E. A.; Alonso, J.; Kubiak, P.; Luisa Fdez-Gubieda, M.; Rojo, T. Sodium Distribution and Reaction Mechanisms of a Na3V 2O2(PO4)2F Electrode during Use in a Sodium-Ion Battery. *Chem. Mater.* **2014**, *26* (11), 3391–3402. https://doi.org/10.1021/cm5005104.

(52) Huang, J.; Albero Blanquer, L.; Bonefacino, J.; Logan, E. R.; Alves Dalla Corte, D.; Delacourt, C.; Gallant, B. M.; Boles, S. T.; Dahn, J. R.; Tam, H. Y.; Tarascon, J. M. Operando Decoding of Chemical and Thermal Events in Commercial Na(Li)-Ion Cells via Optical Sensors. *Nat. Energy* **2020**, *5* (9), 674–683. https://doi.org/10.1038/s41560-020-0665-y.

Graphical Abstract